nature geoscience

SUPPLEMENTARY INFORMATION

DOI: 10.1038/NGEO2122

Evidence for oxygenic photosynthesis half a billion years before the Great Oxidation Event

Method Summary:

Rocks were collected from either drill core or surface outcrop without obvious weathering. Exterior surfaces were removed. Samples were powdered in a tungsten carbide mill from chips that were picked to avoid veins. Major element concentrations were determined using either an ICP-MS (Agilent 7500ce Series, or Thermo Element2) or an ICP-AES (Iris Advantage) after a three-acid dissolution or a metaborate fusion, respectively. Accuracy and precision for major element analyses was based on duplicates of the geostandards IF-G, SDO-1, and BHVO-1, and estimated error is less than 5%. For Mo isotopes, powdered samples were digested with concentrated HNO_3 + HF and HNO_3 + HCl, and then the samples were evaporated and dissolved with 7 mol/L HCl.

A portion of this acid solution was doped with Mo double spike and passed through chromatographic columns. Each sample was doped according to the Mo concentration to keep a constant sample/spike ratio. Mo separation was achieved using a two-stage column procedure: a first stage of anion resin separating Mo and most Fe from the matrix, and a second stage of cation exchange separating Mo from remaining Fe. Blanks and duplicates were run in each set of columns. Mo isotope compositions were analyzed using a Thermo Neptune MC-ICP-MS instrument at the Pole Spectrometry Ocean, Brest at IFREMER (France). We used a ^{97}Mo-^{100}Mo double spike solution prepared gravimetrically from Oak Ridge Laboratory metal powders. Optimization of the double spike isotope composition gave ^{95}Mo/^{98}Mo, ^{97}Mo/^{98}Mo and ^{100}Mo/^{98}Mo isotopic ratios of 0.278, 16.663 and 15.704, respectively. Data reduction was done according to Ref. 1, where iterations were repeated until the difference in the δ^{98}Mo value between two consecutive iterations was smaller than 0.001 ‰. The typical number of iterations was ≤ 4. Molybdenum concentrations of samples were constant in each session but varied between sessions from 50 to 200ppb, depending on the Mo content of the sample powders. Molybdenum concentrations were recalculated with the isotope dilution method using the isotopic data and the concentration of double spike added. The MC-ICP-MS instrument was operated at low resolution with an ApexQ desolvating nebulizer, and all Mo isotope masses were measured together with ^{91}Zr and ^{99}Ru in order to monitor isobaric interferences. During each session we performed frequent measurements of our lab Mo standard (Mo SPEX lot 11-177Mo), NIST-3137 standard, and Johnson Matthey Specpure® Mo plasma standard (Lot #802309E; also known as RochMo2) used in previous studies[2], giving $\delta^{98/95}Mo_{SPEX} = \delta^{98/95}Mo_{NIST3137} - 0.37 \pm 0.06$‰ and $\delta^{98/95}Mo_{SPEX} = \delta^{98/95}Mo_{RochMo2} - 0.04 \pm 0.04$‰, respectively. The typical error on each measurement was 0.1‰ (2σ) (see SI Table 1). Error based on duplicate samples was < 0.15‰. Mo isotopic composition is reported using the common δ notation, where δ^{98}Mo (‰) = $[(^{98}Mo/^{95}Mo)_{sample}/(^{98}Mo/^{95}Mo)_{SPEX} - 1]\cdot 1000$. Iron isotope work was also done using a Thermo Neptune MC-ICP-MS instrument at the Pole Spectrometry Ocean, Brest at IFREMER (France). A Ni spike was used for mass bias correction and standard solutions were run every four samples. The typical error on each measurement was 0.05‰ (2σ). Fe isotopic compositions are reported using the common δ notation, where $\delta^{56}Fe(‰) = [(^{56}Fe/^{54}Fe)_{sample}/(^{56}Fe/^{54}Fe)_{IRMM\text{-}14} - 1]\cdot 1000$.

DOI: 10.1038/NGEO2122

For laser ablation work major elements were first measured by electron microprobe (JOEL 8900), while trace element analyses were performed using a Perkin Elmer Elan6000 quadrupole ICP-MS using a New Wave Research UP213 laser ablation system (55 μM spot size) for grain-by-grain analysis of siderite and magnetite at University of Alberta. Full method details are given in Ref. 3. In sum, optimization of ICP-MS instrument parameters (RF power 1200W, peak hopping acquisition, 50 ms dwell time) was achieved by ablating the NIST 612 international glass standard. For quantitative trace element determinations, the NIST 612 standard and BIF samples were ablated using identical conditions with spot sizes of 55 μm, 5 Hz repetition rate and energy density of ~13 J/cm^2. Quantitative results were obtained via the calibration of relative element sensitivities against the NIST 612 standard, and normalization of each analysis to the electron microprobe data for Fe as the internal standard. Data reduction and concentration determinations were obtained using the GLITTER® (XP version, New Wave Research) laser ablation software.

For each sample set Repeated analysis (n=10) of the NIST 612 using a 55 μm spot size yielded relative standard deviations of between 5 and 8% (2 sigma level).

Spot analyses of carbonate cation compositions were done on carbon-coated polished thin sections using a Cameca SX-100 electron microprobe (EMP) at the Spectrau centre of the University of Johannesburg. Operating conditions were 15 kV acceleration, 6 nA beam current, 20 μm spot size and 24 to 68s total counting time (depending on the element). Almandine (Al), diopside (Si), hematite (Fe), periclase (Mg), calcite (Ca), rhodonite (Mn), $BaSO_4$ (Ba) and ZnS (Zn) were used as standard materials. Powder X-ray diffraction (XRD) data were collected on a Rigaku Ultima IV using Cu-kα radiation at Lawrence University. Quantitative analyses were done on the PDXL software package using the Rietveld whole powder pattern fitting method.

Background of examined units:

ca. 2.95 Ga Sinqeni Formation, Pongola Supergroup, South Africa

The Pongola Supergroup is a volcano-sedimentary sequence deposited at ca. 3.0-2.85 Ga on the southeastern margin of the Kaapvaal Craton. It is exposed in the Mpumalanga and KwaZulu-Natal provinces of South Africa and Swaziland, and is, in part, correlative with the Witwatersrand Supergroup of South Africa[4]. Our samples are from the Sinqeni Formation at the base of the largely sedimentary Mozaan Group (SI Fig. 1) and come from two localities (coordinates S28°13.88; E031°11.81 (TSB07-26 samples, drill core) and 28°15.35; E31°13.22 (PG and PO samples, outcrop) in the White Mfolozi Inlier. The Mozaan Group sediments were deposited on a broad marine shelf during thermal subsidence of the Pongola basin. The Sinqeni Formation consists of quartz arenite, shale, and minor conglomerate and iron formation (SI Fig. 1, 2) packaged into two major sandstone sequences separated by a ~12 m thick succession of shale and iron formation (Vlakhoek shale Member). The succession was deposited on a shallow starved outer shelf during a time of maximum transgression[4]. The sampled iron formation is ~3m thick and contains poorly defined magnetite-hematite mesobands with some silica-rich early diagenetic nodules. The iron formation is well laminated with alternations of silica- and magnetite-rich layers and carbonate-rich layers. This iron formation overlies dark-grey shales with locally intercalated ripple-laminated, fine-grained sandstones and is, in turn, overlain by ferrugineous green shale. The age for the Mozaan Group is based on U–Pb zircon dates for rhyolites within the Nsuze Group, which underlies the Mozaan Group[5], a pre-folding quartz porphyry sill that intruded the Mozaan Group[6], and, more recently, a detailed SIMS zircon study of Mozaan Group volcanics and intrusive granitoids[7]. The Sinqeni Formation in sampled drillcore and outcrop sections of the White Mfolozi Inlier has experienced greenschist facies metamorphism, with peak metamorphism prior to - 2.6 Ga [8,9]. The Pongola Supergroup is intruded by extensive, ca. 2.8 to 2.7 Ga old granites that have a significantly different, lower grade metamorphic history than the Pongola sedimentary rocks[9].

The iron formations consist largely of quartz, iron oxides and carbonates and minor silicate and manganese-rich phases (SI Fig. 3). Quantitative mineralogy is presented in SI Table 2. There is both hematite and magnetite in most samples, although hematite is rare in more Mn-rich samples. Magnetite is coarse-grained (typically >50 μm) and sometimes contains (Mn-rich) carbonate inclusions, while the hematite is typically fine-grained (SI Fig. 3). Based on XRD and microprobe work (SI Fig. 4), there are three types of carbonates in the examined samples: siderite, ankerite and Mn-rich kutnahorite (SI Fig. 4). Siderite is the main carbonate phase. Ripidolite, ferrosillite, and Mn-rich garnet (spessartine) are the main silicate phases. For the iron formation, the most significant mineralogical change during peak metamorphism appears to have been formation of metamorphic silicates and secondary Fe and Mn phases. Magnetite and ankerite are typically coarse-grained phases that, together with spessartine, likely formed during the peak of metamorphism. In sections of the Sinqeni Formation in southern Swaziland that experienced up to granulite facies metamorphic conditions, the manganese is likewise present in spessartine[10]. Coarse-grained ankerite appears to have formed at the expense of the siderite and, during this process, Mn was excluded. The siderite contains up to 10 mol% Mn and is typically more Mn-rich than the adjacent metamorphic ankerite (SI Fig. 4). The Mn excluded from the Mn-rich siderite during metamorphic recrystallization appears to be retained as spessartine and, potentially, as the Mn-rich kutnahorite. Although the coarse 'floating' idiomorphic magnetite grains certainly

formed during metamorphism, no petrographic evidence pinpoints a single formation pathway. For instance, the magnetite could have formed either from a siderite or a hematite precursor[11]. Although Fe-carbonate thermal decomposition is typically thought to be associated with graphite formation, it is possible to have magnetite formation without carbon retention during greenschist facies metamorphism[11]. The presence of carbonate inclusions in some of the magnetite grains suggests a carbonate precursor for some of the magnetite. In a greenschist metamorphic grade oxide-facies iron formation both magnetite formation pathways are possible.

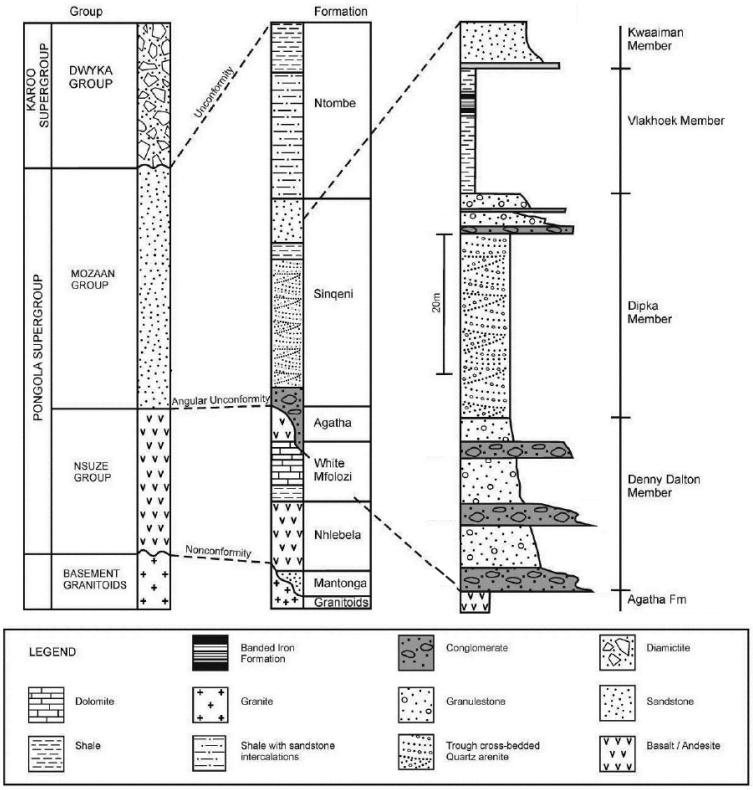

SI Figure 1. Overview of the stratigraphy of the Pongola Supergroup. Modified from Ref. 12.

It is important to consider the ultimate vector of Mo sequestration within sediments during deposition of the Sinqueni Formation. Based on reflected light petrography and SEM and XRD work, the examined intervals have a paucity of sulfide phases. This suggests that there was limited sulfide-mediated sequestration of Mo shuttled to the sediment pile by metal oxides. In other words, seawater-derived Mo that was released into the porewaters from Mn and Fe oxide surfaces during oxide dissolution was unlikely to have been converted to tetrathiomolybdate and scavenged, similar to what is commonly observed in the modern marine sediments. This process can lead to sediment Mo isotope signatures indicative of Mn redox cycling. However, some of the Mo released into the porewaters during formation of the Sinqeni iron formation would have been incorporated into early diagenetic carbonates. Laser ablation work (SI Figure 5; SI Table 3) confirms this view; siderite and magnetite—early diagenetic and metamorphic phases, respectively—both contain significant amounts of Mo. Because the original Mo isotope fractionation linked with Mo-Mn oxide interactions is imposed through a sorption process, there is no reason to surmise an isotope fractionation associated with the diagenetic remobilization of this Mo. Further, there is no straightforward reason to posit a large Mo isotope fractionation associated with Mo incorporation into carbonates, given that there is no coordination change and no change in redox state, assuming molybdate replaces the carbonate ion. This early diagenetic process—metal oxide shuttling of Mn into porewaters, oxide dissolution, and early diagenetic carbonate precipitation—should thus lead to a correlation between sediment Mn contents and Mo isotope values.

Similar to most Precambrian successions, within the examined sequence there are some secondary veins (e.g., calcite veins). However, they have a very localized effect and are not altering the bulk rock geochemical signatures. Furthermore, sections of the unit with late-stage

alteration features were avoided. Overall, the mineralogy of the examined samples reflects secondary (metamorphic) mineral formation from recrystallization of an early diagenetic mineral assemblage dominated by metal oxides and carbonates. Like all Archean rocks, these units have experienced significant burial alteration. However, there is no petrographic evidence that suggest they cannot be used as paleoceanographic archives. Importantly, petrographic evidence indicates an Archean origin for the observed Mn-enrichment and it is inconsistent with the possibility of extensive late-stage oxic alteration.

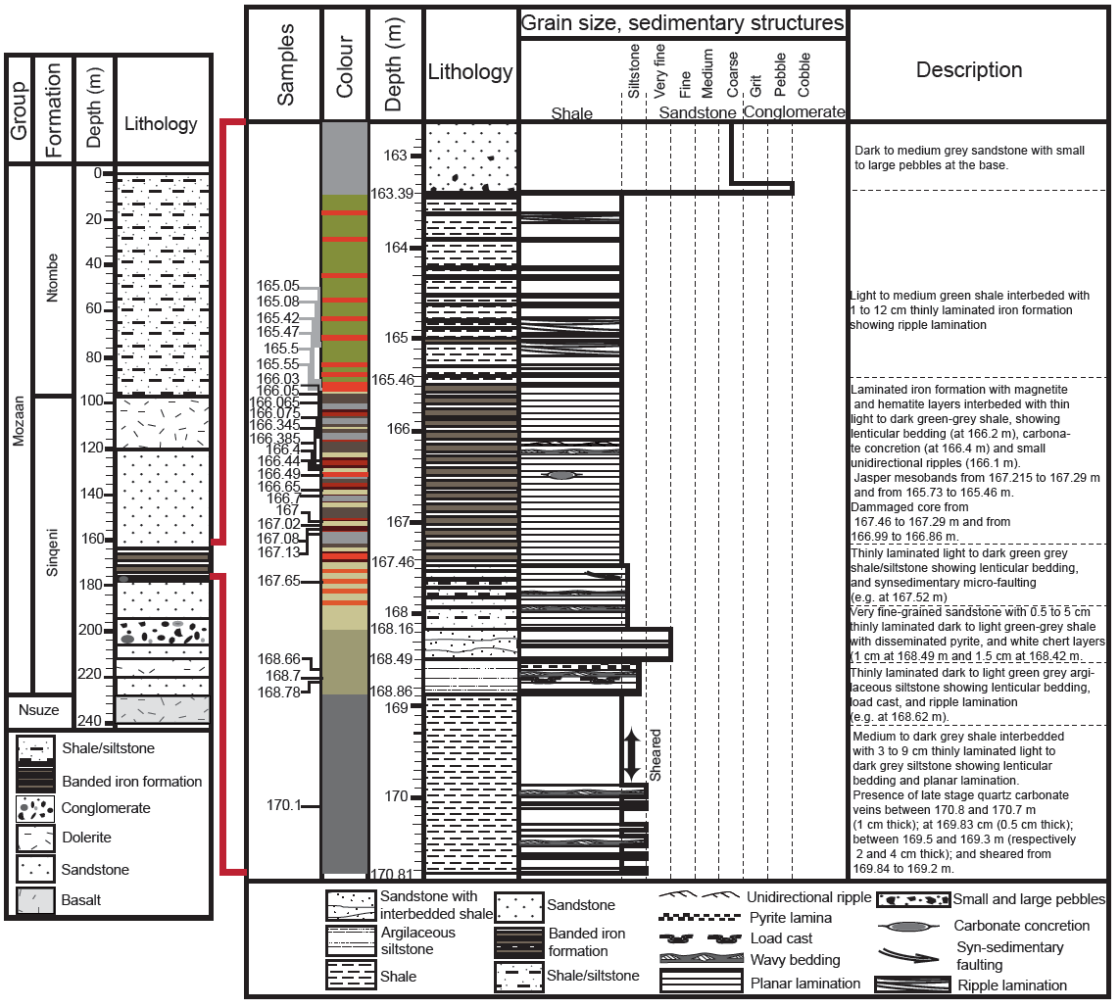

SI Figure 2. Stratigraphy and sedimentology of the interval investigated in drill core (TSB07-26).

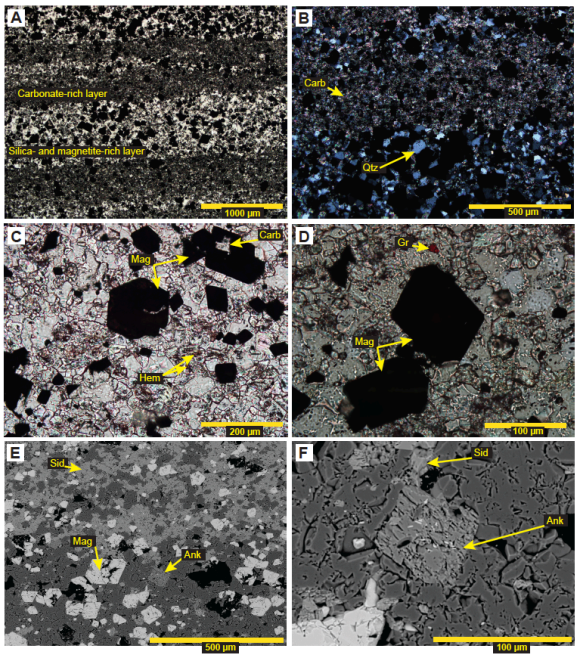

SI Figure 3. Petrography of the Sinqeni iron formation. A-B. Representative view of fine-scale laminations found through much of the unit. Laminations are defined by varying amounts of magnetite, silica, and iron carbonates. C. Coarse-grained magnetite grains. Note the carbonate inclusion (Carb) in the magnetite grain. Hematite (Hem) is finer-grained than adjacent magnetite (Mag). D. Coarse-grained magnetite and garnet (Gr) in a quartz matrix. E-F. Backscatter electron images showing the distribution and grain size of iron carbonate phases. Siderite, the most common carbonate phase, is fine-grained (relative to magnetite and ankerite), and does not typically occur as discrete, idiomorphic grains (unlike magnetite and ankerite).

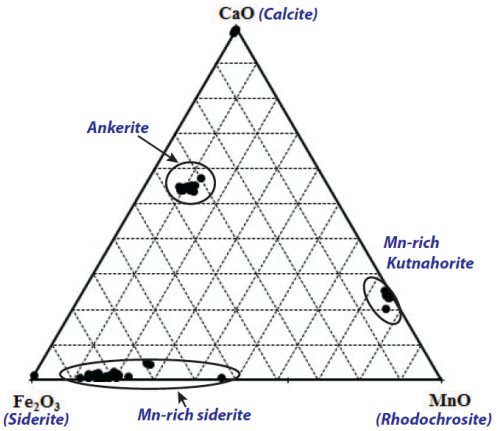

SI Figure 4. Ternary diagram of carbonate phases from the Sinqeni iron formation based on microprobe cation concentrations. Carbonate phases contain significant amounts of Mn (except for late-stage pure calcite veins), notably siderite and Mn-rich kutnahorite on average contain more Mn than ankerite.

As discussed in the main text, iron isotope systematics can be used to assess the degree to which distillation linked to water column iron cycling controlled the δ^{98}Mo values[13]. As iron oxidation proceeds the dissolved MoO_4^{2-} will become progressively isotopically heavier while the aqueous Fe(II) pool will become isotopically lighter. The aqueous Fe(II) pool will be transferred to the sediments with no fractionation in the case of quantitative oxidation or with a positive fractionation when there is partial oxidation. Mo sorbed to iron oxides will be more negative than the dissolved Mo. Therefore, when a spread of Mo isotope values in a sequence of sediments is linked to progressive iron oxidation in an overlying water mass a negative correlation between sediment δ^{56}Fe and δ^{98}Mo values is predicted[13]. In contrast to what has been observed in some other Archean units with variable δ^{98}Mo values[13], there is a weak positive correlation between δ^{98}Mo and δ^{56}Fe values (SI Figure 6), which suggests that water column iron cycling was not the sole or dominant control on sediment δ^{98}Mo values. The REE and Fe isotope systematics of the Sinqeni Iron Formation were also recently discussed in Refs. 14-16.

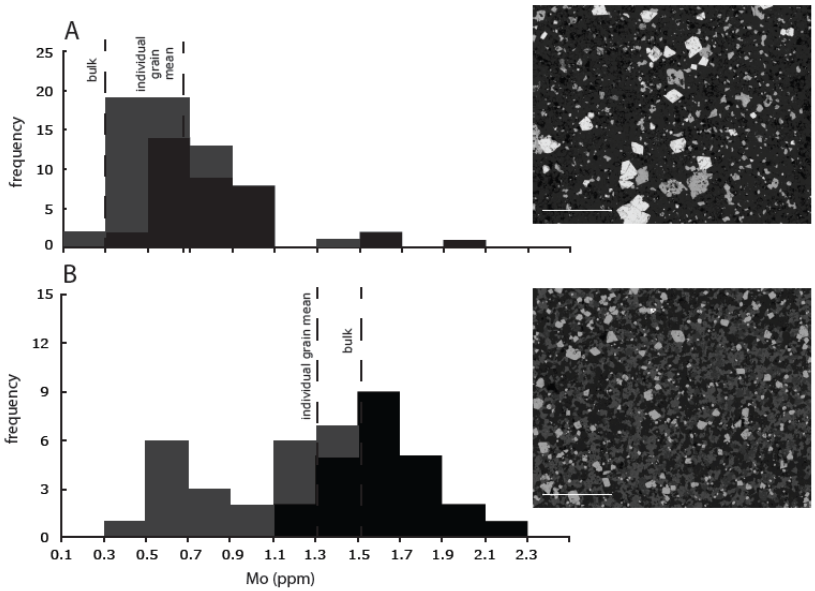

SI Figure 5. Laser-ablation ICP-MS data from individual siderite (dark-grey) and magnetite (light-grey) grains from two representative samples (PG-9-2.05 (A) and TSB07-26-166.4 (B)) that show Mo isotope evidence for Mn oxidation. Magnetite data on the left is shown in black and siderite data is shown in grey. Scale bars are 250 μm.

ca. 2.95 Ga Parktown Formation, Witwatersrand Supergroup, South Africa

One iron formation sample from the Witwatersrand Supergroup examined for this study (IF-9) belongs to the Contorted Bed of the Parktown Formation, Hospital Hill sub-group. The iron formation has a sharp basal contact and a gradational upper contact and is up to 13 m thick. It sits within a shale and shale-siltstone succession and represents the condensed section at the base of an upward-coarsening cycle[17]. The iron formation is composed of a magnetite-rich lower part with hematite and jasper at the very base and a siderite-rich upper part. This iron formation likely correlates with the Scotts Hill iron formation of the Mozaan Group stratigraphically above the Singeni iron formation (SI Fig 6). The age of the Witwatersrand Supergroup is reasonably well constrained by U-Pb ages of overlying and underlying units, detrital zircons, and detrital and authigenic xenotimes[18,19].

Extent of Pongola-Witwatersrand Basin Mn enrichments

Our geochemical and petrographic work focused on a narrow stratigraphic interval (the Sinqeni iron formation, Ijzermijn Member) within a limited geographic region. However, basin-wide studies have indicated that there are several widespread stratigraphic intervals within the Pongola-Witwatersrand Basin that are Mn enriched (e.g., Ref. 20). Specifically, the Promise Formation, the Albida Member, the Blinkpoort Member, the Contorted Bed, the Ntanyana Formation, Neonga Formation, Delfkom Foramtion, Mbhoke Member, and the Water Tower iron formation (See SI Fig. 6) contain more than a half percent Mn, with several weight percent Mn enrichments in most of these intervals (e.g., Ref. 20). Similar to what we found in the Sinqeni iron formation, the Mn is typically found in carbonates and Mn rich garnets, unless the interval has experienced secondary oxide formation[20]. These enrichments are well above typical iron formation and bulk shale values and are most parsimoniously linked to a shuttle of Mn oxides to the sediments[21]. Additionally, it is important to note that most of the Mn enrichments are not stratigraphically linked to the potentially glacially influenced intervals in the Odwaleni and Government subgroups[20] (See SI Fig. 6) and, therefore, cannot be linked to glacially derived oxidants (e.g., peroxide). The Sinqeni is over 1000 m below the potential glacially influenced intervals (See SI Fig. 6).

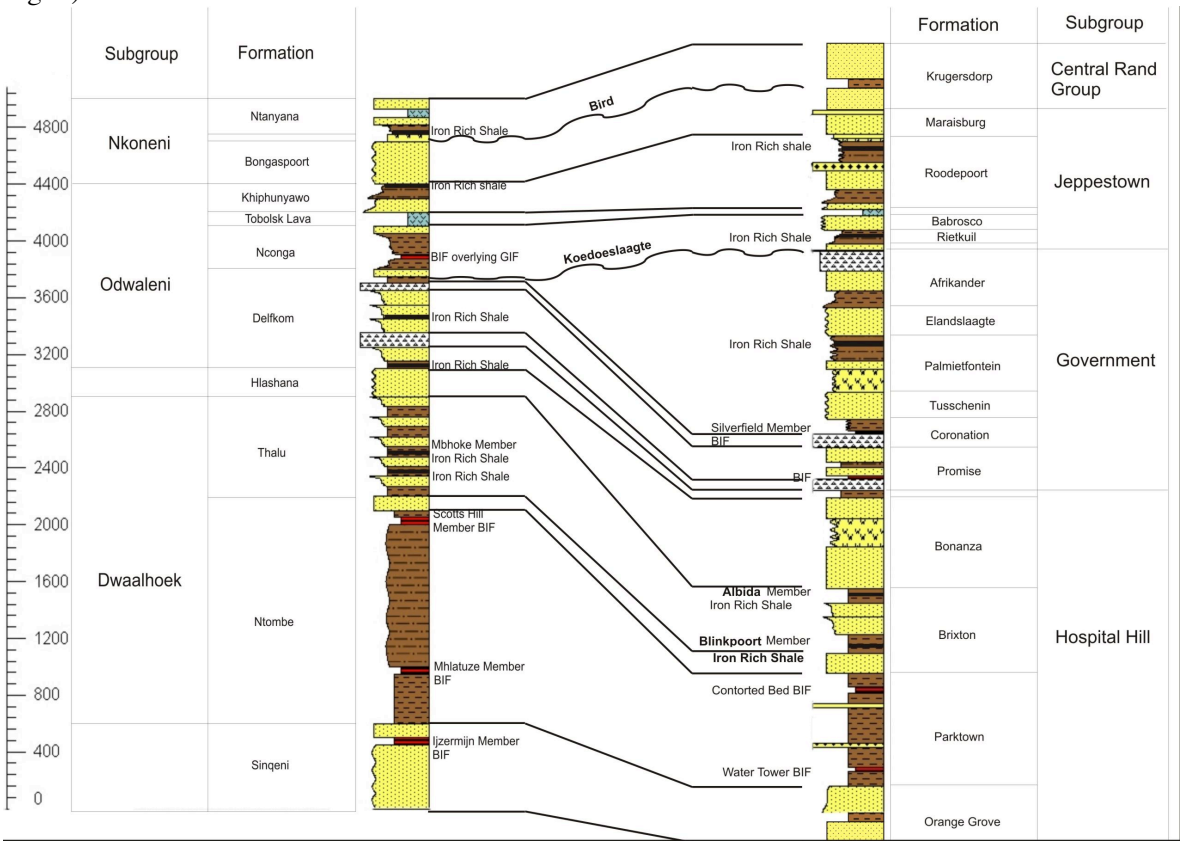

SI Figure 6. Overview of the stratigraphy and tentative correlations within the Pongola-Witwatersrand Basin. Stratigraphic height is in meters. Modified from Ref. 20.

ca. 2.7 Ga Manjeri Formation, Zimbabwe

The Manjeri Formation is a part of the volcano-sedimentary succession of the Belingwe Greenstone Belt, Zimbabwe and overlies older Neoarchean greenstone assemblage and basement gneisses. The Manjeri Formation is up to 250 m thick and contains conglomerates, shallow-water sandstones and stromatolitic limestones grading upwards into shale, graywacke, and iron formation. The iron formation does not appear to be directly linked to volcanic activity associated with the overlying komatiite-basalt sequence, although it is difficult to establish due to unresolved structural complexities. The age of the Manjeri Formation is poorly constrained and may be diachronous along strike. It is younger than an underlying 2831 ± 6 Ma greenstone succession, but older than or in part contemporaneous with a structurally overlying, ca. 2.7 Ga ultramafic to mafic subaqueous lava plain sequence[22,23]. The Manjeri Formation has been correlated with similar successions in other greenstone belts of Zimbabwe[24]. REE and Fe isotope systematics of the same Manjeri iron formation samples were recently described in Refs. 14 and 25.

ca. 2.32 Ga Timeball Hill Formation, South Africa

The Timeball Hill Formation is a part of the Pretoria Group in South Africa. The lower part of the Timeball Hill Formation is composed of pyritic, finely-laminated carbonaceous shales. Depending on the location within the Transvaal basin, the shale transitions upwards into either quartzite/ironstone or ironstone, informally known as the Klapperkop Member. The quartzite/ironstone unit then fines upwards into another suite of finely-laminated carbonaceous shales. The ironstone of the Timeball Hill Formation was deposited in a dynamic depositional environment, likely a shallow-marine to deltaic part of the basin[26-32]. The age of the Timeball Hill formation is best defined by a Re-Os age of 2316 ± 7 Ma from the shales straddling the contact of the Rooihoogte and overlying Timeball Hill formations[28]. Although primary sedimentary structures and textures are well preserved in the Timeball Hill Formation, iron minerals have been recrystallized. The Timeball Hill Formation has experienced lower greenschist facies metamorphism. Trace element and Fe isotope systematics of the Timeball Hill formation were recently discussed in Refs. 3, 14, and 25.

1.88 Ga Biwabik, Gunflint, and Ironwood iron formations, Animikie Basin, USA and Canada

The Paleoproterozoic Animikie basin is located in the Lake Superior area of Canada and USA and contains several geographically separate, but nearly coeval, thick iron formation-bearing sedimentary successions[33]. The basin extends northeastward from the Mesabi Range in north-central Minnesota (containing the Biwabik Iron Formation) to the Gunflint Range in Ontario (containing the Gunflint Iron Formation). The Gogebic, Marquette, and Menominee ranges in north-central Wisconsin and the Upper Peninsula of Michigan lie along the eastern extension of the basin and contain the Ironwood, Negaunee, and Vulcan iron formations. The tectonic model for the Animikie basin has been debated for years. The basin has been interpreted as a foreland basin that formed in response to crustal loading during the Penokean orogeny. More recently, however, an analysis based on syntectonic intrusions and sedimentology has launched the notion that the iron formations were formed in extensional (back-arc) basins north of the subduction zone during the earliest stages in the Penokean orogeny[34,35]. The Gunflint Iron Formation contains the shallowest facies in the basin and is dominated by granular iron formation. All of the iron formations also contain deeper-water, finely-laminated units. There are large massive sulfide deposits within the Animikie basin, but the iron formations are not directly related to them and are distal to volcanic activity, although interlayering of iron formation with mafic and felsic volcanic and volcaniclastic rocks has been documented[34,36]. The Animikie basin iron formations contain a wide range of lithologies, but samples included in this study are Fe carbonate- and Fe oxide-dominated. The age of the Animikie basin sedimentary units is well-constrained by several U-Pb ages on individual zircons[34,36].

Samples used for this study come from several drill core and outcrop exposures in the lower to middle parts of the correlative Gunflint, Negaunee, and Biwabik Iron Formations in Ontario, (Canada), Michigan (USA), and Minnesota (USA), respectively. Sample locality, major and trace

element geochemistry, and Fe isotope systematics of the samples were previously described in Refs. 14,25. Samples that display obvious signs of supergene alteration (e.g., presence of martite or silica leaching) were avoided. The samples come from 'lower slaty' and 'upper cherty' units within the iron formations, covering roughly 100 meters of stratigraphic section[15]. Given that samples span a large stratigraphic interval, there was likely variability in the dissolved δ^{98}Mo values of the seawater from which the iron formation precursor sediments precipitated. Within the proposed model for coupled Mo and metal oxide water column and sediment behavior, temporal seawater δ^{98}Mo variability would lead to a scattering in the sediment Mo isotope and Fe/Mn ratio correlation. This is likely a factor leading the large confidence interval on the linear regression between δ^{98}Mo and Fe/Mn ratios for the Animikie Basin sediments (see below).

Statistical treatment of Fe/Mn – δ^{98}Mo relationship in the studied iron formations:

The data are normally distributed with respect to δ^{98}Mo values with a mean of 0.28‰ (n=42, 1σ =0.72), and log-normally distributed with respect to Fe/Mn with a mean of 225.51 (n=42, 1σ =408.35) (Fig. S7). Thus, for the purpose of regression and significance testing, data were examined in terms of δ^{98}Mo vs. log Fe/Mn.

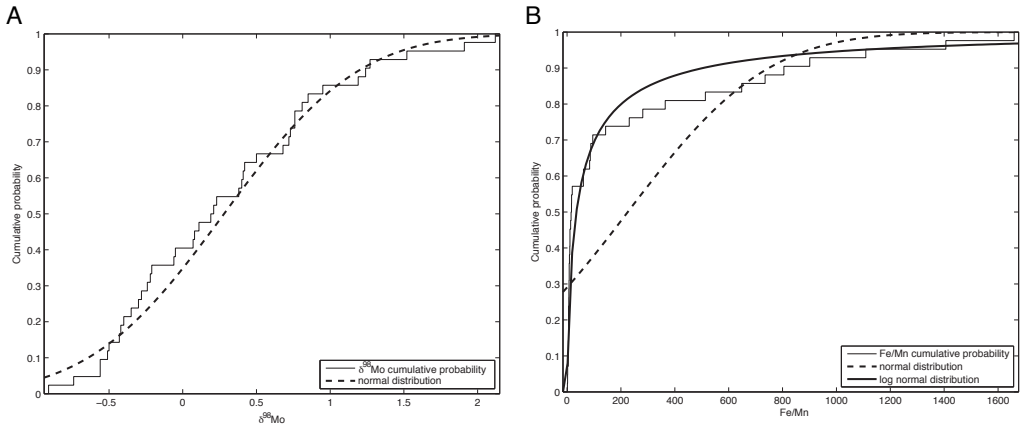

SI Figure 7. Cumulative probability function for δ^{98}Mo values (A) and Fe/Mn ratios (B) and idealized normal distribution (in the case of Fe/Mn ratios, log-normal distribution) calculated from data mean and variance.

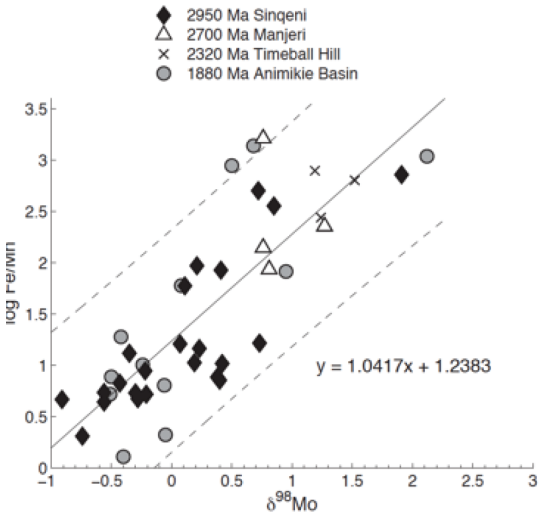

SI Figure S8. Linear regression for the collective dataset and associated 95% confidence intervals.

All data may be fit in δ^{98}Mo vs. log Fe/Mn space by a single regression line of slope 1.04 ± 0.23 and y-intercept of 1.24 ± 0.15 (errors are 2SE) (Figure S6). When the data are regressed individually by formation, a one-way analysis of covariance (ANOCOVA) of their slope differences provides a F-test statistic of 0.70 (p=0.5589, 3 degrees of freedom), indicating that the slopes as a collective are not significantly different.

The limited data available at present for the Manjeri formation (n=3) and for the Timeball Hill formation (n=4) result in relatively restricted ranges for both δ^{98}Mo and Fe/Mn. These formations have little effect on the slope of the data (or resulting F statistic) when regressed collectively, and are thus limited at present in their utility for revealing true differences in coupled δ^{98}Mo-Fe/Mn behavior. In the case of the Sinqeni formation and Animikie basin, however, for which significantly more data is available (n=23 and 12, respectively), their individual slopes when regressed independently are statistically indistinguishable (F-test statistic of 0.77, p=0.3874, 1 degree of freedom)(Figure S7). Therefore, there is no statistical support for differences in δ^{98}Mo-Fe/Mn behavior between data from the Sinqeni formation and Animikie basin.

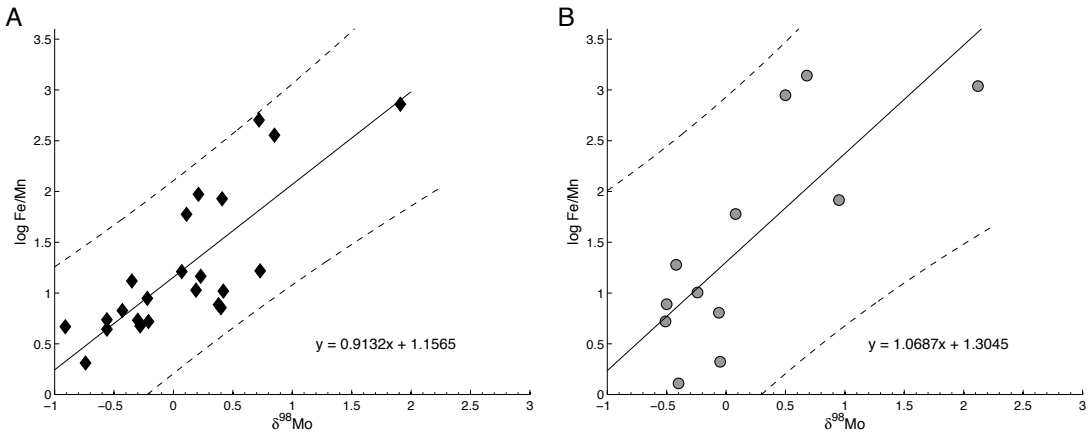

SI Figure 9. Linear regressions and associated 95% confidence intervals calculated independently for (A) the Sinqeni iron formation and (B) Animikie basin iron formations.

References:

1 Siebert, C., Nagler, T. F. & Kramers, J. D. Determination of molybdenum isotope fractionation by double-spike multicollector inductively coupled plasma mass spectrometry. *Geochemistry Geophysics Geosystems* **2**, 2000GC000124 (2001).

2 Anbar, A. D., Knab, K. A. & Barling, J. Precise determination of mass-dependent variations in the isotopic composition of molybdenum using MC-ICP-MS. *Analytical Chemistry* **73**, 1425-1431, Doi 10.1021/Ac000829w (2001).

3 Konhauser, K. O. *et al*. Oceanic nickel depletion and a methanogen famine before the Great Oxidation Event. *Nature* **458**, 750-753 (2009).

4 Beukes, N. J., Cairncross, B., A lithostratigraphic- sedimentological reference profile for the Late Archaean Mozaan Group, Pongola Sequence: application to sequence stratigraphy and correlation with the Witwatersrand Supergroup. *South African Journal of Geology* **94**, 44–69 (1991).

5 Hegner, E., Kroner, A. & Hofmann, A. W. Age and Isotope Geochemistry of the Archean Pongola and Usushwana Suites in Swaziland, Southern-Africa - a Case for Crustal Contamination of Mantle-Derived Magma. *Earth and Planetary Science Letters* **70**, 267-279 (1984).

6 Gutzmer, J., Nhleko, N., Beukes, N. J., Pickard, A. & Barley, M. E. Geochemistry and ion microprobe (SHRIMP) age of a quartz porphyry sill in the Mozaan Group of the Pongola Supergroup; implications for the Pongola and Witwatersrand supergroups. *South African Journal of Geology* **102**, 139-146 (1999).

7 Mukasa, S. B., Wilson, A.H., Young, K.R., . Geochronological Constraints on the Magmatic and Tectonic Development of the Pongola Supergroup (Central Region), South Africa. *Precambrian Research* **224**, 268–286 (2013).

8 Elworthy, T., Eglington, B. M., Armstrong, R. A. & Moyes, A. B. Rb-Sr isotope constraints on the timing of late to post-Archaean tectonometamorphism affecting the southeastern Kaapvaal Craton. *Journal of African Earth Sciences* **30**, 641-650 (2000).

9 Wilson, A. & Jackson, M. Mantled gneiss domes in southern Swaziland and the concept of 'stable' Pongola cratonic cover. *South African Journal of Geology* **91**, 404-414 (1988).

10 Horváth, P., Reinhardt, J., Hofmann, A. and Nagy, G. High-grade metamorphism of ironstones in the Mesoarchaean of southwest Swaziland. *Mineralogy and Petrology* DOI 10.1007/s00710-013-0307-1 (2014).

11 Yui, S. Decomposition of siderite to magnetite at lower oxygen fugacities: a thermochemical interpretation and geological implications. *Economic Geology* **61**, 768-776 (1966).

12 Hicks, N., and Hofmann, A. Stratigraphy and provenance of the auriferous-uraniferous, fluvial to shallow-marine Sinqeni Formation, Mozaan Group, northern KwaZulu-Natal, South Africa. *South African Journal of Geology* **115**, 327-344 (2012).

13 Czaja, A. D. *et al*. Evidence for free oxygen in the Neoarchean ocean based on coupled iron-molybdenum isotope fractionation. *Geochimica et Cosmochimica Acta* **86**, 118-137, (2012).

14 Planavsky, N. J. *et al*. Iron isotope composition of some Archean and Proterozoic iron formations. *Geochimica et Cosmochimica Acta* **80**, 158-169 (2012).

15 Planavsky, N., Bekker, A., Rouxel, O., Knudsen, A. & Lyons, T. W. Rare earth element and yttrium compositions of Archean and Paleoproterozoic iron formations revisited: New perspectives on the significance and mechanisms of deposition. *Geochimica et Cosmochimica Acta* **74**, 6387-6405 (2010).

16 Delvigne, C., Cardinal, D., Hofmann, A., André, L. Stratigraphic changes of Ge/Si, REE+Y and silicon isotopes as insights into the deposition of a Mesoarchaean banded iron formation. *Earth and Planetary Science Letters,* **355**, 109–118 (2012).

17 Frimmel, H. E. Witwatersrand iron-formations and their significance for gold genesis and the composition limits of orthoamphibole. *Mineralogy and Petrology* **56**, 273-295 (1996).

18 Armstrong, R. A., Compston, W., de Wit, M. J. & Williams, I. S. The stratigraphy of the 3.5–3.2 Ga Barberton greenstone belt revisited: A single zircon ion microprobe study. *Earth and Planetary Science Letters* **101**, 90-106 (1990).

19 Kositcin, N. & Krapez, B. Relationship between detrital zircon age-spectra and the tectonic evolution of the Late Archaean Witwatersrand Basin, South Africa. *Precambrian Research* **129**, 141-168 (2004).
20 Smith, A. J. B. *The Paleo-environmental Significance of the Iron- formations and Iron-rich Mudstones of the Mesoarchean Witwatersrand-Mozaan Basin, South Africa*. Masters thesis, University of Johannesburg (2007).
21 Maynard, J. B. in *Treatise of Geochemistry* Vol. 7 (ed F.T. McKenzie) 289-308 (Elsevier-Pergamon, 2004).
22 Hunter, M. A., Bickle, M. J., Nisbet, E. G., Martin, A. & Chapman, H. J. Continental extensional setting for the Archean Belingwe Greenstone Belt, Zimbabwe. *Geology* **26**, 883-886 (1998).
23 Hofmann, A. & Kusky, T. The Belingwe Greenstone Belt: Ensialic or Oceanic? *Developments in Precambrian Geology* **13**, 487–538 (2004).
24 Prendergast, M. D. The Bulawayan Supergroup: a late Archaean passive margin-related large igneous province in the Zimbabwe craton. *Journal of the Geological Soceity of London* **161**, 431-445 (2004).
25 Planavsky, N. J. *et al*. Iron-oxidizing microbial ecosystems thrived in late Paleoproterozoic redox-stratified oceans. *Earth and Planetary Science Letters* **286**, 230-242 (2009).
26 Coetzee, L. L., Beukes, N. J., Gutzmer, J. & Kakegawa, T. Links of organic carbon cycling and burial to depositional depth gradients and establishment of a snowball Earth at 2.3 Ga. Evidence from the Timeball Hill Formation, Transvaal Supergroup, South Africa. *South African Journal of Geology* **109**, 109-122 (2006).
27 Eriksson, P. G. *et al*. Possible evidence for episodic epeiric marine and fluvial sedimentation (and implications for palaeoclimatic conditions), c. 2.3-1.8 Ga, Kaapvaal craton, South Africa. *Palaeogeography, Palaeoclimatology, Palaeoecology* **273**, 153-173, (2009).
28 Hannah, J. L., Bekker, A., Stein, H. J., Markey, R. J. & Holland, H. D. Primitive Os and 2316 Ma age for marine shale: implications for Paleoproterozoic glacial events and the rise of atmospheric oxygen. *Earth and Planetary Science Letters* **225**, 43-52 (2004).
29 Catuneanu, O. & Eriksson, P. G. Sequence stratigraphy of the Precambrian Rooihoogte-Timeball Hill rift succession, Transvaal Basin, South Africa. *Sedimentary Geology* **147**, 71-88 (2002).
30 Catuneanu, O. & Eriksson, P. G. The sequence stratigraphic concept and the Precambrian rock record: an example from the 2.7-2.1 Ga Transvaal Supergroup, Kaapvaal craton. *Precambrian Research* **97**, 215-251 (1999).
31 Eriksson, P. G. & Reczko, B. F. F. Contourites associated with pelagic mudrocks and distal delta-fed turbidites in the Lower Proterozoic Timeball Hill Formation epeiric basin (Transvaal Supergroup), South Africa. *Sedimentary Geology* **120**, 319-335 (1998).
32 Eriksson, P. G. *et al*. Early Proterozoic Black Shales of the Timeball-Hill Formation, South-Africa - Volcanogenic and Paleoenvironmental Influences. *South African Journal of Geology* **18**, 325-337 (1994).
33 Ojakangas, R. W., Morey, G. B. & Southwick, D. L. Paleoproterozoic basin development and sedimentation in the Lake Superior region, North America. *Sedimentary Geology* **141**, 319-341 (2001).
34 Fralick, P., Davis, D. W. & Kissin, S. A. The age of the Gunflint Formation, Ontario, Canada: single zircon U-Pb age determinations from reworked volcanic ash. *Canadian Journal of Earth Sciences* **39**, 1085-1091 (2002).
35 Schulz, K. J. & Cannon, W. F. The penokean orogeny in the lake superior region. *Precambrian Research* **157**, 4-25 (2007).
36 Schneider, D. A., Bickford, M. E., Cannon, W. F., Schulz, K. J. & Hamilton, M. A. Age of volcanic rocks and syndepositional iron formations, Marquette Range Supergroup: implications for the tectonic setting of Paleoproterozoic, iron formations of the Lake Superior region. *Canadian Journal of Earth Sciences* **39**, 999-1012 (2002).

SI Table 1. Isotope data and major element concentrations

Sample Name*	Formation, Group	Age (Ga)	**δ98/95**	2sigma 97/95	Mo (ppb)	**δ56/54**	2sigma 56/54	Fe/Mn	**δ53/52**	2sigma 53/52	Cr (ppm)	Al (%)	Fe (%)	Mn (%)	Ti (ppm)	Mg (%)	Ca (%)
TSB07-26-165.47	Sinqeni Formation, Pongola	2.95	**-0.22**	0.05	2390	**-1.39**	0.06	9	-0.05	0.07	5	0.01	16.7	1.9	7	0.7	0.2
TSB07-26-165.42	Sinqeni Formation, Pongola	2.95	**-0.30**	0.10	308	**-1.55**	0.06	5				0.37	31.7	5.8	-	3.6	0.4
TSB07-26-166.065	Sinqeni Formation, Pongola	2.95	**-0.74**	0.09	950	**-1.44**	0.06	2				1.59	12.3	5.9	-	3.1	1.2
TSB07-26-166.345	Sinqeni Formation, Pongola	2.95	**-0.21**	0.08	857	**-1.61**	0.06	5				1.43	24.1	4.5	-	3.0	2.7
TSB07-26-166.385	Sinqeni Formation, Pongola	2.95	**0.11**	0.06	2179	**-1.71**	0.06	61				0.15	48.8	0.8	-	0.4	0.1
TSB07-26-166.4	Sinqeni Formation, Pongola	2.95	**-0.43**	0.07	1536	**-1.36**	0.06	7	-0.13	0.11	27	0.90	29.5	4.3	200	1.9	1.2
TSB07-26-166.44	Sinqeni Formation, Pongola	2.95	**-0.56**	0.08	1589	**-0.95**	0.06	6				1.31	26.1	4.7	48	2.5	1.9
TSB07-26-166.65	Sinqeni Formation, Pongola	2.95	**-0.28**	0.06	2133	**-0.84**	0.06	5	-0.10	0.06	6	0.04	8.9	1.8	2	0.7	0.1
TSB07-26-167.1	Sinqeni Formation, Pongola	2.95	**0.07**	0.05	4341	**-1.11**	0.06	17				4.80	30.4	1.8	306	1.5	0.2
TSB07-26-167.08	Sinqeni Formation, Pongola	2.95	**-0.91**	0.10	3110	**-1.51**	0.06	5				0.34	26.0	5.5	-	2.2	0.6
TSB07-26-167.65	Sinqeni Formation, Pongola	2.95	**-0.56**	0.09	2460	**-1.07**	0.06	4				0.31	26.2	5.9	-	2.3	0.4
TSB07-26-170.1	Sinqeni Formation, Pongola	2.95	**-0.35**	0.10	1863			13				13.88	5.1	0.4	474	1.0	0.06
PG-3-0.4	Sinqeni Formation, Pongola	2.95	**0.21**	0.05	3707	**-1.05**	0.09	95	-0.09	0.14	7	0.29	49.1	0.5	5	0.05	0.02
PG-5C-1.5	Sinqeni Formation, Pongola	2.95	**0.72**	0.04	9669	**-0.75**	0.09	514	-0.11	0.15	1	0.02	46.7	0.1	5	-	0.02
PG-6C-1.3	Sinqeni Formation, Pongola	2.95	**1.91**	0.17	3277	**-0.70**	0.09	735	-0.11	0.15	1	0.03	47.3	0.1	3	0.01	0.03
PG-7A-1.41	Sinqeni Formation, Pongola	2.95	**0.23**	0.09	178	**-1.15**	0.04	15	-0.15	0.06	1	0.07	3.7	0.2	3	0.02	0.01

PG7C-1.48	Sinqeni Formation, Pongola	2.95	**0.41**	0.09	169	**-1.03**	0.09	86				-	4.4	0.1	-	0.01	0.03
PG-7D-1.52	Sinqeni Formation, Pongola	2.95	**0.40**	0.10	477	**-1.13**	0.09	7	-0.08	0.06	2	0.16	6.5	0.9	4	0.02	0.01
PG-9-2.05	Sinqeni Formation, Pongola	2.95	**0.73**	0.15	285	**-0.93**	0.12	17				-	17.6	1.0	-	0.05	0.03
PO5-1	Sinqeni Formation, Pongola	2.95	**0.38**	0.06	3383	**-0.73**	0.09	8				0.08	18.8	2.4	1	0.01	0.1
PO5-6	Sinqeni Formation, Pongola	2.95	**0.19**	0.05	1532	**-1.53**	0.08	11				0.13	25.0	2.3	2	0.05	0.1
P05-7	Sinqeni Formation, Pongola	2.95	**0.42**	0.07	883	**-0.64**	0.04	11	0.09	0.12	12	0.09	11.2	1.1	1	0.04	0.2
IF-9	Parktown Formation, Witwatersrand	2.95	**0.85**	0.05	80	**0.04**	0.07	365				0.19	25.9	0.07	6	0.03	0.03
Z04-12	Manjeri Iron Formation	2.7	**0.76**	0.06	94	**0.86**	0.09	1660				0.07	15.7	0.01	5	0.01	0.2
ZO4-13	Manjeri Iron Formation	2.7	**1.27**	0.04	527	**-1.17**	0.11	231				0.11	1.0	0.004	67	0.00	0.02
ZO4-31	Manjeri Iron Formation	2.7	**0.76**	0.04	359	**0.79**	0.06	143				0.11	21.5	0.2	2	0.09	0.3
ZO4-32	Manjeri Iron Formation	2.7	**0.81**	0.05	230	**0.85**	0.07	88				0.04	8.9	0.1	0.5	0.26	0.3
B36-2001-M5	Timeball Hill Formation	2.35	**1.24**	0.03	23714	**-0.19**	0.02	281				3.07	38.3	0.1	198	0.09	0.1
B36-2001-M9B2	Timeball Hill Formation	2.35	**1.19**	0.04	19674	**-0.01**	0.01	805				2.88	55.4	0.07	131	0.04	0.1
B36-4-2001-M9B1	Timeball Hill Formation	2.35	**1.52**	0.02	10682	**0.01**	0.05	648				3.24	43.6	0.07	141	0.02	0.05
317-12	Biwabik Iron Formation, Animikie	1.88	**0.08**	0.05	2420	**-0.22**	0.09	61				0.90	53.9	0.9	93	1.53	1.2
317-13	Biwabik Iron Formation, Animikie	1.88	**-0.05**	0.05	1244	**-0.66**	0.09	2				0.04	15.5	7.2	1	1.51	2.4

317-20	Biwabik Iron Formation, Animikie	1.88	**-0.50**	0.05	1447	**0.25**	0.06	8	0.10	3.0	0.4	3	0.21	0.2
317-8	Biwabik Iron Formation, Animikie	1.88	**-0.42**	0.05	1129	**0.15**	0.04	19	0.55	36.6	1.9	56	2.74	5.8
DE-ONC-1	Biwabik Iron Formation, Animikie	1.88	**-0.51**	0.15	229			5	5.45	5.5	1.0	3999	4.08	0.7
DH3-27	Gunflint Iron Formation, Animikie	1.88	**0.95**	0.04	827	**0.64**	0.05	84	0.12	26.4	0.3	6	0.25	11.4
DH3-42	Gunflint Iron Formation, Animikie	1.88	**0.50**	0.05	415			901	5.95	23.3	0.03	473	1.72	0.2
DH3-43	Gunflint Iron Formation, Animikie	1.88	**0.68**	0.06	475			1406	4.19	28.0	0.02	355	1.62	0.5
DI3	Ironwood Iron Formation, Animikie	1.88	**2.12**	0.12				1109	0.19	33.3	0.03	11	0.08	0.03
EM-MN-1	Biwabik Iron Formation, Animikie	1.88	**-0.06**	0.13	482	**-0.29**	0.01	6	0.04	12.6	1.9	2	8.90	0.1
UT-J-1	Biwabik Iron Formation, Animikie	1.88	**-0.40**	0.11	1113	**-0.50**	0.06	1	0.03	9.1	7.0	1	0.97	0.6
UT-J-2	Biwabik Iron Formation, Animikie	1.88	**-0.24**	0.05	872	**1.10**	0.06	10	0.05	10.7	1.0	6	0.11	0.1

*For Pongola samples the number at the end of the code marks the stratigraphic position. For PG-samples it is the meters below the top of the Vlakhoek Member of the Sinqeni Formation

Major element data from Refs. 24-25

SI Table 2. Quantitative mineralogy*

Sample	χ^2	Quartz	Hematite	Mn-rich Kutnahorite	Mn-rich Siderite	Magnetite	Ankerite	Spessartine	Ferrosilite	Ripidolite
TSB07-26-166.03	2.11	15.9 (6)	4 (5)	5 (1)	44 (1)	2.7 (4)	8.0 (6)	0.4 (7)	19 (1)	1.1 (6)
TSB07-26-166.65 (3)	2.49	85.5 (7)	3.2 (2)	6.7 (3)	0.0 (2)	0.2 (4)	0.0(7)	-	0 (1)	4 (2)
TSB07-26-165.47	3.00	80.3 (5)	1.6 (1)	-	17.3 (3)	0.8 (1)	-	-	-	-
TSB07-26-165.42	2.39	14.9 (8)	0.4 (2)	13 (3)	61 (1)	0.3 (3)	6 (3)	0.9 (7)	0 (1)	4 (1)
TSB07-26-166.345	1.77	22 (4)	0.7 (4)	0.1 (5)	30.9 (5)	2.2 (2)	44 (2)	-	-	-
TSB07-26-166.385	2.56	66 (1)	0.8 (2)	8 (2)	7 (1)	16.9 (4)	0.4 (3)	-	0 (1)	-
TSB07-26-166.44	2.04	33.8 (6)	1.6 (7)	5 (4)	29.1 (6)	5.0 (4)	16.8 (9)	-	1.2 (4)	7 (1)
TSB07-26-166.4	2.25	37.7 (7)	-	6 (1)	35.3 (8)	5.5 (4)	2.4 (3)	0.4 (6)	9.5 (1)	2.0 (8)
TSB07-26-167.65	2.28	16.4 (4)	0.3 (7)	2.4 (6)	34.1 (7)	6 (3)	1.2 (7)	-	35 (6)	5.3 (6)
TSB07-26-167.02	2.34	33.0 (8)	5 (1)	7.3 (7)	15 (3)	9.7 (5)	1 (1)	2.9 (3)	0.9 (5)	25 (1)
TSB07-26-168.78	1.73	33.9 (5)	8 (2)	6 (2)	46 (1)	1.1 (1)	5 (2)	-	1 (1)	-
PG-3	1.58	59.7 (9)	26.6 (6)	-	-	13.7 (5)	-	-	-	-
PG-6A	2.15	74.2 (9)	20.4 (7)	-	-	4.8 (7)	0.5 (3)	0.06 (3)	-	-
PG-6C	1.63	72.1 (8)	24.9 (5)	-	-	2.7 (3)	0 (3)	0.03 (4)	0 (1)	-
PG-7B	2.69	95.6 (6)	1.4 (2)	0.0 (1)	1.3 (8)	0.7 (8)	0.3 (2)	-	-	-
PG-7D	2.48	95.4 (6)	2.3 (2)	0.1 (1)	0.2 (3)	1.0 (2)	0.3 (8)	1 (1)	-	-
PG-8	2.62	84.6 (8)	2.8 (4)	-	-	4.6 (8)	-	1 (1)	-	-

*The χ^2-value represents the overall quality of the analysis for each sample. Values are reported in percentages.

*The parenthetical value represents the reported error in the last decimal place.

SI Table 3. Mo concentration (ppm) in individual mineral grains determined by LA-ICP-MS

PG-9-2.05 - siderite	PG-9-2.05 - magnetite	TSB07-26-166.4-siderite	TSB07-26-166.4-Magnetite
0.8	1.1	0.6	0.8
0.9	1.3	0.5	0.6
0.6	1.5	0.6	1.1
1.0	1.5	1.5	2.1
1.3	2.1	0.4	0.6
1.3	1.9	0.4	0.5
1.2	1.5	0.8	1.6
0.9	1.8	0.3	0.6
0.7	1.7	0.3	0.6
0.7	1.8	0.4	0.6
0.6	1.5	0.4	0.6
1.1	1.6	0.7	1.0
1.1	1.6	0.4	0.6
1.0	1.4	0.4	0.7
1.4	2.1	0.7	0.9
0.5	1.8	0.3	0.9
0.6	1.6	0.6	1.0
0.6	1.6	0.4	0.7
0.5	1.6	0.4	0.7
	1.2	0.3	0.6
	1.4	0.4	0.6
	2.3	0.4	0.6
	1.6	0.8	1.1
	1.6	0.6	1.0
	1.6	0.8	1.6
		0.2	0.5
		0.5	0.7
		0.7	0.9
		0.4	0.5
		0.5	0.7
			1.0
			0.6
			1.0
			0.8
			0.8
			0.9
			0.9